yeast. Liquid culture densities were equalized using absorption at 600 nm, and 10 µl of each dilution was spotted on to histidine minus medium before incubation.

Vesicle analysis

Vesicle analysis was performed on leaf segments stained with DAB to detect H_2O_2 as described[15]. Leaves of 7-day-old seedlings were inoculated with *B. g. hordei*, and 24 h later they were assessed by differential interference contrast microscopy for vesicles in the short cells of the adaxial epidermis[23]. Per genotype, 100 sites were scored from each of three leaves. Only sites at which penetration had failed were scored.

See Supplementary Information for barley genotype analysis with *B. g. hordei*, and PEN1 and ROR2 localization.

Received 16 June; accepted 15 September 2003; doi:10.1038/nature02076.

1. Johnson, L. E. B., Bushnell, W. R. & Zeyen, R. J. Defense patterns in nonhost higher plant species against two powdery mildew fungi. I. Monocotyledonous species. *Can. J. Bot.* **60,** 1068–1083 (1982).
2. Freialdenhoven, A., Peterhänsel, C., Kurth, J., Kreuzaler, F. & Schulze-Lefert, P. Identification of genes required for the function of non-race-specific *mlo* resistance to powdery mildew in barley. *Plant Cell* **8,** 5–14 (1996).
3. Hoogkamp, T. J. H., Chen, W. Q. & Niks, R. E. Specificity of prehaustorial resistance to *Puccinia hordei* and to two inappropriate rust fungi in barley. *Phytopathology* **88,** 856–861 (1998).
4. Mellersh, D. G., Foulds, I. V., Higgins, V. J. & Heath, M. C. H_2O_2 plays different roles in determining penetration failure in three diverse plant-fungal interactions. *Plant J.* **29,** 257–268 (2002).
5. Hammond-Kosack, K. E. & Parker, J. E. Deciphering plant-pathogen communication: fresh perspecitives for molecular resistance breeding. *Curr. Opin. Biotechnol.* **14,** 177–193 (2003).
6. Peterhänsel, C., Freialdenhoven, A., Kurth, J., Kolsch, R. & Schulze-Lefert, P. Interaction analyses of genes required for resistance responses to powdery mildew in barley reveal distinct pathways leading to leaf cell death. *Plant Cell* **9,** 1397–1409 (1997).
7. Sanderfoot, A. A., Assaad, F. F. & Raikhel, N. V. The *Arabidopsis* genome. An abundance of soluble *N*-ethylmaleimide-sensitive factor adaptor protein receptors. *Plant Physiol.* **124,** 1558–1569 (2000).
8. Blatt, M. R. Toward understanding vesicle traffic and the guard cell model. *New Phytol.* **153,** 405–413 (2002).
9. Jahn, R., Lang, T. & Südhof, T. C. Membrane fusion. *Cell* **112,** 519–533 (2003).
10. Fasshauer, D., Sutton, R. B., Brunger, A. T. & Jahn, R. Conserved structural features of the synaptic fusion complex: SNARE proteins reclassified as Q- and R-SNAREs. *Proc. Natl Acad. Sci. USA* **95,** 15781–15786 (1998).
11. Shen, Q. H. *et al.* Recognition specificity and RAR1/SGT1 dependence in barley *Mla* disease resistance genes to the powdery mildew fungus. *Plant Cell* **15,** 732–744 (2003).
12. Lerman, J. C., Robblee, J., Fairman, R. & Hughson, F. M. Structural analsysis of the neuronal SNARE protein syntaxin-1A. *Biochemistry* **39,** 8470–8479 (2000).
13. Munson, M., Chen, X., Cocina, A. E., Schultz, S. M. & Hughson, F. M. Interactions within the yeast t-SNARE Sso1p that control SNARE complex assembly. *Nature Struct. Biol.* **7,** 894–902 (2000).
14. Misura, K. M. S., Scheller, R. H. & Weis, W. I. Self-association of the H3 region of syntaxin 1A. *J. Biol. Chem.* **276,** 13273–13282 (2001).
15. Hückelhoven, R., Fodor, J., Preis, C. & Kogel, K. H. Hypersensitive cell death and papilla formation in barley attacked by the powdery mildew fungus are associated with hydrogen peroxide but not with salicylic acid accumulation. *Plant Physiol.* **119,** 1251–1260 (1999).
16. Lauber, M. H. *et al.* The *Arabidopsis* KNOLLE protein is a cytokinesis-specific syntaxin. *J. Cell Biol.* **139,** 1485–1493 (1997).
17. Betz, W. J. & Richards, D. A. What goes out must come in. *Nature Neurosci.* **3,** 636–637 (2000).
18. Emans, N., Zimmerman, S. & Fischer, R. Uptake of fluorescent marker in plant cells is sensitive to brefeldin A and wortmannin. *Plant Cell* **14,** 71–86 (2002).
19. Lamb, C. & Dixon, R. A. The oxidative burst in plant disease resistance. *Annu. Rev. Plant Physiol. Plant Mol. Biol.* **48,** 251–275 (1997).
20. Snyder, B. A. & Nicholson, R. L. Synthesis of phytoalexins in sorghum as a site-specific response to fungal ingress. *Science* **248,** 1637–1639 (1990).
21. Adam, L. & Somerville, S. C. Genetic characterization of five powdery mildew disease resistance loci in *Arabidopsis thaliana*. *Plant J.* **9,** 341–356 (1996).
22. Yu, Y. *et al.* A bacterial artificial chromosome library for barley (*Hordeum vulgare* L.) and the identification of clones containing putative resistance genes. *Theor. Appl. Genet.* **101,** 1093–1099 (2000).
23. Koga, H., Bushnell, W. R. & Zeyen, R. J. Specificity of cell type and timing of events associated with papilla formation and the hypersensitive reaction in leaves of *Hordeum vulgare* attacked by *Erysiphe graminis* f. sp *hordei*. *Can. J. Bot.* **68,** 2344–2352 (1990).
24. Sutton, R. B., Fasshauer, D., Jahn, R. & Brunger, A. T. Crystal structure of a SNARE complex involved in syntaptic exocytosis at 2.4 Å resolution. *Nature* **395,** 347–353 (1998).

Supplementary Information accompanies the paper on **www.nature.com/nature**.

Acknowledgements This work was supported by Syngenta, the Max Planck Society, the Gatsby Charitable Foundation, the Danish Agricultural and Veterinary Research Council, the GABI Non-host Resistance Consortium (Bundesministerium für Bildung und Forschung), the Carnegie Institution of Washington, and the US Department of Energy. M.S. was supported in part by a Stanford Graduate Fellowship. N.C.C. thanks the host group of K. Shirasu in the Sainsbury Laboratory. We thank R. Bradbourne and H. Tippmann for technical assistance; M. Gale for microsatellite primers; M. Miklis and J. Uhrig for silencing and yeast two-hybrid vectors; R. Serrano and R. Napier for H^+-ATPase and CALRETICULIN antisera; and R. Oliver for the GUS reporter construct.

Competing interests statement The authors declare that they have no competing financial interests.

Correspondence and requests for materials should be addressed to P.S.-L. (schlef@mpiz-koeln.mpg.de). Sequences are deposited in GenBank under accession numbers AY246893 to AY246907 and AY247208 to AY247214.

Bone recognition mechanism of porcine osteocalcin from crystal structure

Quyen Q. Hoang[1,2], Frank Sicheri[3,4], Andrew J. Howard[5] & Daniel S. C. Yang[1]

[1]*Department of Biochemistry, Faculty of Health Science, McMaster University, Hamilton, Ontario L8N 3Z5, Canada*
[2]*Microstar Biotech Inc., 7 Innovation Drive, Flamborough, Ontario L9H 7H9, Canada*
[3]*Program in Molecular Biology and Cancer, Samuel Lunenfeld Research Institute, Mount Sinai Hospital, 600 University Avenue, Toronto, Ontario M5G 1X5, Canada*
[4]*Department of Molecular and Medical Genetics, University of Toronto, Toronto, Ontario M5S 1A8, Canada*
[5]*Department of Biological, Chemical and Physical Sciences, Illinois Institute Technology, Chicago, Illinois 60616, USA*

Osteocalcin is the most abundant noncollagenous protein in bone[1], and its concentration in serum is closely linked to bone metabolism and serves as a biological marker for the clinical assessment of bone disease[2]. Although its precise mechanism of action is unclear, osteocalcin influences bone mineralization[3,4], in part through its ability to bind with high affinity to the mineral component of bone, hydroxyapatite[5]. In addition to binding to hydroxyapatite, osteocalcin functions in cell signalling and the recruitment of osteoclasts[6] and osteoblasts[7], which have active roles in bone resorption and deposition, respectively. Here we present the X-ray crystal structure of porcine osteocalcin at 2.0 Å resolution, which reveals a negatively charged protein surface that coordinates five calcium ions in a spatial orientation that is complementary to calcium ions in a hydroxyapatite crystal lattice. On the basis of our findings, we propose a model of osteocalcin binding to hydroxyapatite and draw parallels with other proteins that engage crystal lattices.

The primary structure of osteocalcin (OC) is highly conserved among vertebrates and contains three vitamin-K-dependent γ-carboxylated glutamic acid (Gla) residues at positions 17, 21 and 24 in porcine OC (pOC; Fig. 1a and Supplementary Fig. 1). Solution studies have shown that mature OC is largely unstructured in the absence of calcium and undergoes a transition to a folded state on the addition of physiological concentrations of calcium[8]. NMR analysis has shown that OC is a globular protein consisting of α-helical secondary structure in its folded state[8,9], but the detailed three-dimensional structure of OC has not been forthcoming.

To gain further insight into the structure of OC and its ability to recognize the hydroxyapatite (HA) mineral component of bone, we have determined the crystal structure of pOC at 2.0 Å using the Iterative Single Anomalous Scattering method[10]. Bijvoet difference Patterson map analysis detected the presence of three tightly bound Ca^{2+} ions and two S atoms corresponding to a disulphide bridge between Cys 23 and Cys 29, which together were used to phase the pOC structure. An atomic model corresponding to residues Pro 13 to Ala 49 was built into well-defined electron density (Supplementary Fig. 2) and refined to an R_{work} and R_{free} of 25.5% and 28.3%, respectively. Data collection and structure refinement statistics are summarized in Supplementary Table 1.

pOC forms a tight globular structure comprising a previously unknown fold (no matches in the DALI database[11]) with a topology consisting, from its amino terminus, of three α-helices (denoted α1–α3) and a short extended strand (denoted Ex1; Fig. 1b). Helix α1 and helix α2 are connected by a type III turn structure from Asn 26 to Cys 29 and form a V-shaped arrangement that is stabilized

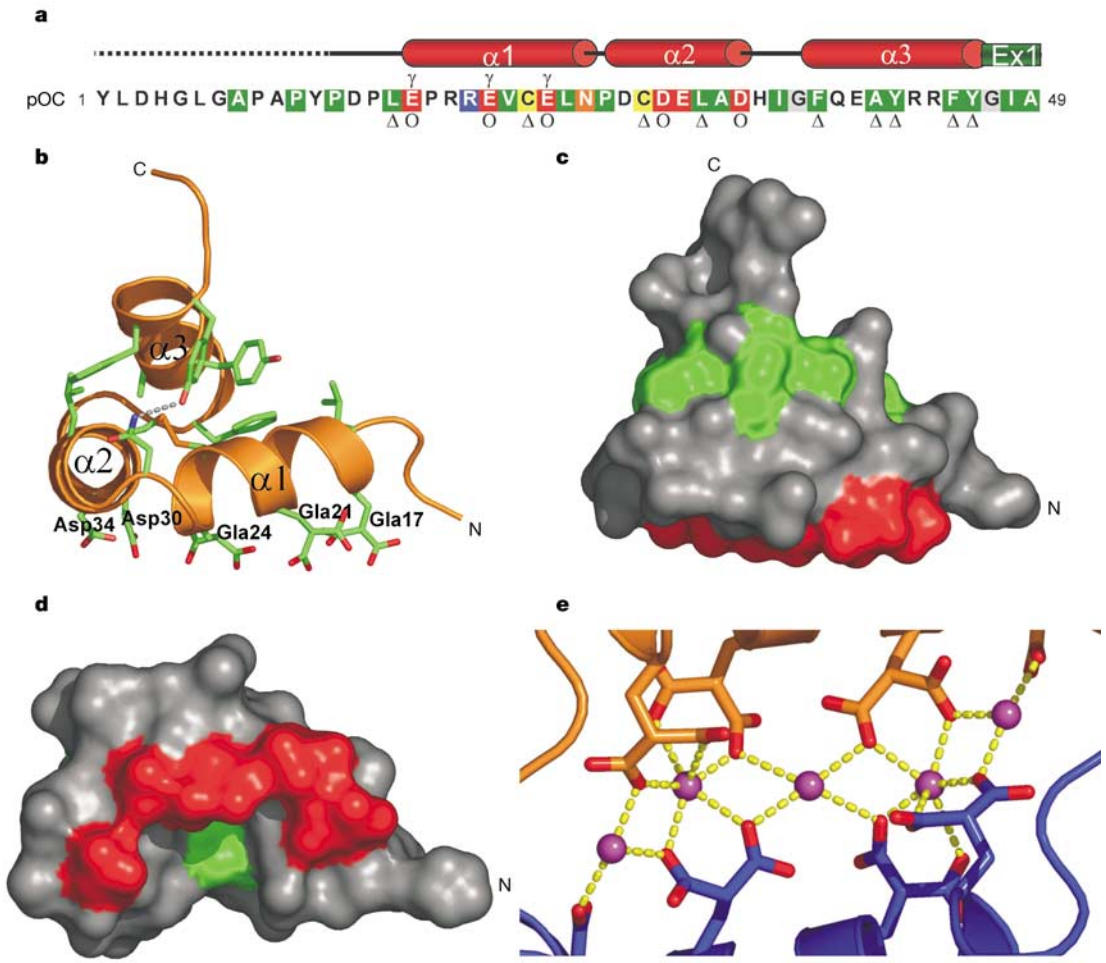

Figure 1 Structure of pOC. **a**, Protein sequence with the secondary structure elements indicated and the conserved residues highlighted (green, red, blue, yellow, orange and grey indicate conserved, acidic, basic, cysteine, asparagine and glycine residues, respectively). Positions are identified as conserved if more than 85% of the residues are identical, or similar if hydrophobic in nature (see Supplementary Information for the full sequence alignment). 'γ' indicates a Gla residue, open triangles and circles indicate hydrophobic core and Ca^{2+}-coordinating surface, respectively. **b**, Ribbon representation of the crystal structure. The N and C termini are labelled. Side chains of the Ca^{2+}-coordinating residues and those involved in tertiary structure stabilization are shown in stick representation. Broken grey line indicates a hydrogen bond. **c**, **d**, Molecular surface representations of pOC with the surface hydrophobic patch (green) and the Ca^{2+}-coordinating surface (red) highlighted. Views in **b** and **c** are perpendicular to that in **d**. **e**, Crystallographic dimer interface. Orange and blue distinguish the two molecules. Purple spheres and the yellow broken lines represent Ca^{2+} ions and ionic bonds, respectively.

by an interhelix disulphide bridge involving Cys 23 and Cys 29. Helix α3 is connected to helix α2 by a short turn and is aligned to bisect the V-shape arrangement of helix α1 and helix α2. The three α-helices together compose a tightly packed core involving conserved hydrophobic residues Leu 16, Leu 32, Phe 38, Ala 41, Tyr 42, Phe 45 and Tyr 46. The overall tertiary structure is further stabilized by a hydrogen bond interaction between two invariant residues, Asn 26 in the helix α1–α2 linker and Tyr 46 in helix α3.

Projection of conserved residues onto the molecular surface of the pOC structure (Fig. 1c, d) shows an extensive negatively charged surface centring on helix α1 (solvent-exposed surface area 586 $Å^2$). Notably, all three Gla residues implicated in HA binding are located on the same surface of helix α1 and, together with the conserved residue Asp 30 from helix α2, coordinate five Ca^{2+} ions (denoted Ca1–Ca5) in an elaborate network of ionic bonds (Fig. 1e). These five Ca^{2+} ions are sandwiched between two crystallographically related pOC molecules and show both monodentate and malonate modes of chelation with extensive bridging.

In the pOC crystal structure, the Ca^{2+} ions coordinated by the Gla residues have an unexpected periodic order reminiscent of a crystalline lattice. Because Gla residues are essential for the interaction of OC with bone *in vivo*[12] and for the specific interaction with HA *in vitro*[5], we investigated whether the specific atomic arrangement of bound Ca^{2+} ions in the pOC crystal structure mimics the spatial arrangement of Ca^{2+} ions in HA. To do so, we carried out a comprehensive real-space search for a spatial match between the pOC-bound Ca^{2+} ions and the Ca^{2+} ions in crystalline HA ($Ca_5(PO_4)_3OH$, space group $P6_3/m$, unit-cell dimensions $a = b = 9.432$ Å, $c = 6.881$ Å)[13]. Search solutions were ranked by root mean square (r.m.s.) deviations of distances between OC-bound and HA Ca^{2+} ions.

Unique solutions within 1 s.d. (0.29 Å) of the best solution were chosen for graphical analysis. Molecular surfaces of HA defined by the Ca^{2+} ions of our best search solutions were constructed for docking analysis (Fig. 2 and Supplementary Fig. 3). The best (r.m.s. deviation 0.44 Å) and fourth best (r.m.s. deviation 0.62 Å) solutions in our search correspond to the prism face (100) of HA, whereas the second (r.m.s. deviation 0.47 Å) and third (r.m.s. deviation 0.61 Å) best solutions correspond to the secondary prism face (110). Notably, the prism face is the predominant crystal face expressed in geological[14] and synthetic HA[15] and, although the predominant crystal face of HA expressed in bone has not been unambiguously

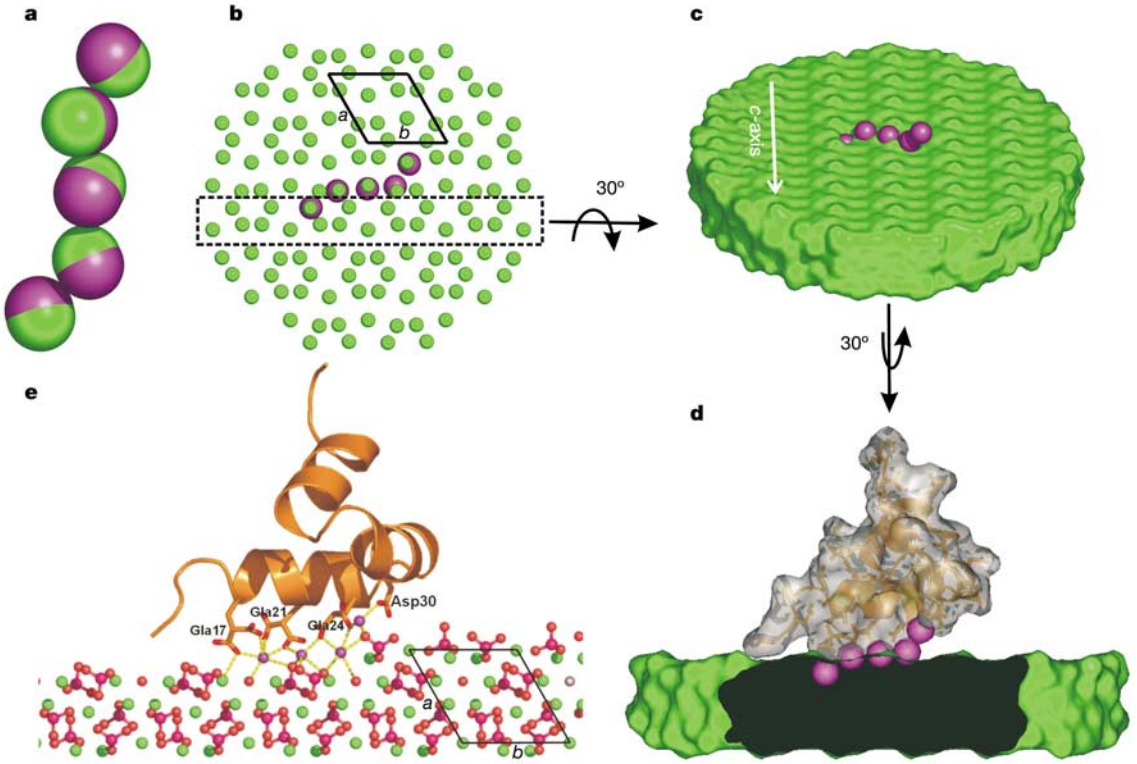

Figure 2 Model of pOC engaging an HA crystal based on a Ca^{2+} ion lattice match. Only the best search solution is shown (see Supplementary Information for a comparison of the four best solutions). **a**, Alignment of pOC-bound (purple) and HA (green) Ca^{2+} ions. **b**, **c**, Orientation of pOC-bound Ca^{2+} ions in a sphere of HA–Ca lattice (**b**) and on the HA surface (**c**). In **b**, the parallelogram indicates a unit cell; the box approximates the boundary of the slab shown in **c** and **d**. **d**, Docking of pOC (orange backbone with grey semitransparent surface) on HA. **e**, Detailed view of **d** showing the Ca–O coordination network at the pOC–HA interface. Yellow broken lines denote ionic bonds. Isolated red spheres and the tetrahedral clusters of magenta and red spheres represent OH^- and PO_4^{3-} ions, respectively.

determined, atomic force microscopy[16] and diffraction analysis[17] indicate that the expressed face lies parallel to the crystal *c* axis. The best solution identified in our search also corresponds to a crystal face that lies parallel to the crystal *c* axis.

Although the best and second best solutions both show good lattice match statistics, only the best solution gives rise to a docking mode of pOC to HA that is free of steric clash. Using our best search solution, we generated a more detailed binding model. The coordination network of Ca–O atoms at the OC–HA interface closely mimics that in the HA crystal lattice (r.m.s. deviation Ca–O bond distance, 0.19 Å; r.m.s. deviation Ca–O–Ca bond angle, 9.63°; Fig. 2e).

The HA lattice binding mode represented by our best solution presupposes that OC engages HA with the acidic Ca^{2+}-coordinating surface as a monomer. In the crystal structure of pOC, however, the five Ca^{2+} ions are sandwiched between two crystallographically related protein molecules. If overly stable, this dimeric state could present an impediment to HA binding. To investigate whether pOC exists as a monomer or dimer in solution, we carried out sedimentation equilibrium analysis in the presence and absence of 10 mM $CaCl_2$. In both cases, the sedimentation equilibrium data were best fitted to a monomer–dimer equilibrium model (Supplementary Fig. 4). The extrapolated dissociation constants (K_d) for the OC dimer were 8×10^{-4} M and 2×10^{-4} M in the absence and presence of 10 mM $CaCl_2$, respectively. Theses K_d values are 2–3 orders of magnitude higher than the concentration of OC in human serum (0.9×10^{-6} to 7×10^{-16} M)[2], suggesting that OC exists as a monomer *in vivo*.

The crystal structure of pOC provides a first glimpse of the underlying interactions that may constitute biomineral recognition. The recognition of crystal lattices by proteins is important in many biological processes, including the inhibition of ice crystal growth and the development of teeth, bone and shells. The best-characterized protein–crystal recognition system studied so far corresponds to the interaction of antifreeze proteins (AFP) with ice[18,19]. AFPs bind to the surface of ice to modify crystal morphology and to inhibit ice growth. AFPs with different three-dimensional structures bind to different planes of ice, and the shape complementarity between the ice-binding surface of AFP and the ice crystal surface to which it binds is the primary determinant for binding specificity.

The excellent surface complementarity between the Ca^{2+}-coordinating surface of pOC and the prism face of HA suggests that pOC may also show selective binding characteristics to HA. By analogy to the antifreeze proteins, the binding of OC to HA could directly modulate HA crystal morphology and growth. In addition, when OC is bound to the surface of HA, other regions, including the carboxy terminus of the protein, which possesses chemotactic activity[20], would be well orientated to carry out recruitment and signal transduction functions through binding to cell surface receptors on osteoclasts[6] and osteoblasts[7]. The structure of pOC provides a model for further functional analyses. □

Methods

Protein purification and crystallization

We purchased fresh porcine bone from the local market. Preparation of bone powder and extraction of acid-soluble proteins were done as described[21]. OC was purified to homogeneity from the acid extract by using Sep-Pak C_{18} cartridges (No. WAT043345, Waters), followed by reverse-phase HPLC using a Delta Pak C_{18} column (No. WAT011799, Waters). Protein purity was assessed by SDS–PAGE and analytical reverse-phase HPLC with a Delta Pak C_{18} column (No. 011797, Waters). Protein authenticity was determined by mass spectrometry (relative molecular mass 5,737) and amino acid composition. We obtained protein yields of 10 mg of pure OC from 30 g of bone powder.

Lyophilized OC was dissolved in 100 mM HEPES (pH 7.4) to a concentration of 10 mg ml^{-1} (estimated by absorbance at 280 nm). We grew crystals at room temperature

by vapour diffusion from hanging drops made of equal volumes (2.5 μl) of protein and a reservoir solution of 0.1 M HEPES, 10 mM $CaCl_2$ and 10% (w/v) PEG 4000, pH 7.4. Crystals of the space group $P3_121$ with a unit-cell dimension of $a = 51.5$ Å, $b = 51.5$ Å and $c = 35.4$ Å grew overnight.

Crystallographic data collection and structure determination

All data were collected at beamline 17-ID of the Advanced Photon Source at Argonne National Laboratory. The X-ray wavelength was set at 1.7 Å. We cryo-cooled OC crystals in a nitrogen cold stream after transferring them to a cryo-protectant containing 30% PEG 4000, 10 mM $CaCl_2$ and 0.1 HEPES, pH 7.4. Diffraction data were collected at 100 K on an Mar165 CCD detector (MarUSA) and processed with the program HKL[22]. Two data sets, each covering 180° rotation, were merged to increase data redundancy. Three Ca^{2+} ions and two S atoms were located and used for phase determination with the program SOLVE[23]. We improved phases by solvent flattening with the program RESOLVE[24]. The program O[25] was used for model building. Refinement was done with CNS[26] using maximum-likelihood targets. The N-terminal 12 residues are disordered and so excluded from the final model.

Modelling of OC binding to HA

To determine the HA crystal surface to which OC might bind, we wrote a Fortran program that constructs a HA lattice and carries out real-space searches. The Ca^{2+} ions at the pOC dimer interface were used as a search model as follows. First, each atom of the search model was systematically placed onto each of the two unique Ca^{2+} ions of the HA crystal lattice. Each placement then served as a pivot point on which the search model was rotated (as a rigid body to preserve the atomic arrangement) about three eulerian axes ($\theta_1, \theta_2, \theta_3$) at increments of 5° over the ranges $0° < \theta_1 < 360°$, $0° < \theta_2 < 360°$ and $0° < \theta_3 < 360°$. After each rotational increment, the search model was refined by least squares to the closest HA Ca^{2+} ions and the r.m.s. deviation in distance between the search model and HA Ca^{2+} ions was calculated. We sorted the unique solutions according to their r.m.s. deviation values and selected solutions within 1 s.d. of the best solution for graphical analysis. Slabs of the HA lattice corresponding to putative binding planes defined by the search solutions were constructed and pOC was docked by using the program LSQKAB[27] of the CCP4 (ref. 28) package.

For graphical drawing and analysis, the programs O[25] and Pymol[29] were used throughout.

Sedimentation equilibrium analysis

Sedimentation equilibrium experiments of OC in the presence and absence of Ca^{2+} at loading concentrations of 0.17, 0.23 and 0.52 mg ml^{-1} were done at 20 °C on a Optima XL-I analytical ultracentrifuge with AN60TI rotor (Beckman). Samples were prepared by dissolving freeze-dried protein into buffer (0.1 M HEPES and 0.2 M NaCl, with or without 10 mM $CaCl_2$) that had been pretreated with Chelex 100. Data were acquired as an average of ten absorbance measurements at a nominal wavelength of 280 nm and a radial spacing of 0.002 cm at rotor speeds of 45,000, 50,000 and 55,000 r.p.m. Equilibrium was achieved within 16 h. We analysed data in terms of reversible monomer–dimer formation to obtain an estimate of K_d. The partial specific volume of pOC and the solvent density were calculated by the program SedNterp[30]. Global data fits were obtained by simultaneously fitting nine sets of data to a monomer–dimer equilibrium using Origin 6.0 software (Microcal).

Received 7 July; accepted 15 September 2003; doi:10.1038/nature02079.

1. Hauschka, P. V., Lian, J. B., Cole, D. E. C. & Gundberg, C. M. Osteocalcin and matrix Gla protein: vitamin K-dependent proteins in bone. *Physiol. Rev.* **69,** 990–1047 (1989).
2. Calvo, M. S., Eyre, D. R. & Caren, M. G. Molecular basis and clinical application of biological markers of bone turnover. *Endocr. Rev.* **17,** 333–368 (1996).
3. Hauschka, P. V. & Reid, M. L. Timed appearance of a calcium-binding protein containing γ-carboxyglutamic acid in developing chick bone. *Dev. Biol.* **65,** 431–436 (1978).
4. Ducy, P. *et al.* Increased bone formation in osteocalcin-deficient mice. *Nature* **382,** 448–452 (1996).
5. Poser, J. W. & Price, P. A. A method for decarboxylation of γ-carboxyglutamic acid in proteins. *J. Biol. Chem.* **254,** 431–436 (1979).
6. Chenu, C. *et al.* Osteocalcin induces chemotaxis, secretion of matrix proteins, and calcium-mediated intracellular signaling in human osteoclast-like cells. *J. Biol. Chem.* **127,** 1149–1158 (1994).
7. Bodine, P. V. & Komm, B. S. Evidence that conditionally immortalized human osteoblasts express an osteocalcin receptor. *Bone* **25,** 535–543 (1999).
8. Atkinson, R. A. *et al.* Conformational studies of osteocalcin in solution. *Eur. J. Biochem.* **232,** 515–521 (1995).
9. Dowd, T. L., Rosen, J. F., Li, L. & Gundberg, C. M. The three-dimensional structure of bovine calcium ion-bound osteocalcin using ^{1}H NMR spectroscopy. *Biochemistry* **42,** 7769–7779 (2003).
10. Wang, B.-C. Resolution of phase ambiguity in macromolecular crystallography. *Methods Enzymol.* **115,** 90–112 (1985).
11. Hohm, L. & Sander, C. Protein structure comparison by alignment of distance matrices. *J. Mol. Biol.* **233,** 123–138 (1993).
12. Pastoureau, P., Vergnaud, P., Meunier, P. J. & Delmas, P. D. Osteopenia and bone-remodeling abnormalities in warfarin-treated lambs. *J. Bone Miner. Res.* **8,** 1417–1426 (1993).
13. Kay, M. I., Young, R. A. & Posner, A. S. The crystal structure of hydroxyapatite. *Nature* **204,** 1050–1052 (1964).
14. Klein, C. & Hurlbut, C. S. *Manual of Mineralogy* 21st edn (Wiley, New York, 1999).
15. Onuma, K., Ito, A., Tateishi, T. & Kameyama, T. Growth kinetics of hydroxyapatite crystal revealed by atomic force microscopy. *J. Cryst. Growth* **154,** 118–125 (1995).
16. Eppell, S. J., Tong, W., Katz, J. L., Kuhn, L. & Glimcher, M. J. Shape and size of isolated bone mineralites measured using atomic force microscopy. *J. Orthop. Res.* **19,** 1027–1034 (2001).
17. Ziv, V., Wagner, H. D. & Weiner, S. Microstructure–microhardness relations in parallel-fibered and lamellar bone. *Bone* **18,** 417–428 (1996).
18. Davies, P. L., Baardsnes, J., Kuiper, M. J. & Walker, V. K. Structure and function of antifreeze proteins. *Phil. Trans. R. Soc. Lond. B* **357,** 927–935 (2002).
19. Yang, D. S. *et al.* Identification of the ice-binding surface on a type III antifreeze protein with a 'flatness function' algorithm. *Biophys. J.* **74,** 2142–2151 (1998).
20. Mundy, G. R. & Poser, J. W. Chemotactic activity of the γ-carboxyglutamic acid-containing protein in bone. *Calcif. Tissue Int.* **35,** 164–168 (1983).
21. Colombo, G., Fanti, P., Yao, C. & Halluche, H. H. Isolation and complete amino acid sequence of osteocalcin from canine bone. *J. Bone Miner. Res.* **8,** 733–743 (1993).
22. Otwinowski, Z. & Minor, W. Processing of X-ray diffraction data collected in oscillation mode. *Methods Enzymol.* **276,** 307–326 (1997).
23. Terwilliger, T. C. & Berendzen, J. Automated MAD and MIR structure solution. *Acta Crystallogr. D* **55,** 849–861 (1999).
24. Terwilliger, T. C. Maximum-likelihood density modification. *Acta Crystallogr. D* **56,** 1863–1871 (1999).
25. Jones, T. A., Zou, J. Y., Cowan, S. W. & Kjeldgaard, M. Improved methods for building protein models in electron density maps and the location of errors in these models. *Acta Crystallogr. A* **47,** 110–119 (1991).
26. Brunger, A. T. *et al.* Crystallography & NMR system: a new software suite for macromolecular structure determination. *Acta Crystallogr. D* **54,** 905–921 (1998).
27. Kabsch, W. A solution for the best rotation to relate two sets of vectors. *Acta Crystallogr. A* **32,** 922–923 (1976).
28. Collaborative Computational Project Number 4. The CCP4 Suite: programs for protein crystallography. *Acta Crystallogr. D* **50,** 760–763 (1994).
29. DeLano, W. L. *The PyMOL Molecular Graphics System* (DeLano Scientific, San Carlos, 2002).
30. Laue, T. M., Shah, B. D., Ridgeway, T. M. & Pelletier, S. L. *Biochemistry and Polymer Science* (Royal Society of Chemistry, London, 1992).

Supplementary Information accompanies the paper on **www.nature.com/nature**.

Acknowledgements We thank A. Viinberg for assistance with purification; M. Pereira and R. Ghirlando for help with sedimentation equilibrium data acquisition and data analysis, respectively; and W.-C. Hon for comments on the manuscript. Use of the IMCA-CAT beamline 17-ID at the Advanced Photon Source was supported by the companies of the Industrial Macromolecular Crystallography Association through a contract with Illinois Institute of Technology. Use of the Advanced Photon Source was supported by the US Department of Energy, Office of Science, Office of Basic Energy Sciences. This work was supported by the Natural Sciences and Engineering Research Council (NSERC) of Canada.

Competing interests statement The authors declare that they have no competing financial interests.

Correspondence and requests for materials should be addressed to D.S.C.Y.. (yang@mcmaster.ca). The coordinates of the structure are deposited in the Protein Data Bank under accession code 1Q8H.

ATP-dependent reduction of cysteine–sulphinic acid by *S. cerevisiae* sulphiredoxin

Benoît Biteau[1], Jean Labarre[2] & Michel B. Toledano[1]

[1]*Laboratoire Stress Oxydants et Cancer, and* [2]*Laboratoire de Physiogénomique, SBGM, DBJC, CEA-Saclay, 91191 Gif-sur-Yvette cedex, France*

Proteins contain thiol-bearing cysteine residues that are sensitive to oxidation, and this may interfere with biological function either as 'damage' or in the context of oxidant-dependent signal transduction. Cysteine thiols oxidized to sulphenic acid are generally unstable, either forming a disulphide with a nearby thiol or being further oxidized to a stable sulphinic acid[1,2]. Cysteine–sulphenic acids and disulphides are known to be reduced by glutathione or thioredoxin in biological systems, but cysteine–sulphinic acid derivatives have been viewed as irreversible protein modifications. Here we identify a yeast protein of relative molecular mass M_r = 13,000, which we have named sulphiredoxin (identified by the US spelling 'sulfiredoxin', in the *Saccharomyces* Genome Database), that is conserved in higher eukaryotes and reduces cysteine–sulphinic acid in the yeast peroxiredoxin Tsa1. Peroxiredoxins are ubiquitous thiol-containing antioxidants that reduce hydroperoxides[3–5] and con-